

# Synaptic delays shape dynamics and function in multimodal neural motifs

Cite as: Chaos 35, 043106 (2025); doi: 10.1063/5.0233640

Submitted: 16 August 2024 · Accepted: 14 March 2025 ·

Published Online: 1 April 2025






View Online



Export Citation



CrossMark

Xinxin Qie,<sup>1,a)</sup>  Jie Zang,<sup>1,b)</sup>  Shenquan Liu,<sup>1,c)</sup>  and Andrey L. Shilnikov<sup>2,d)</sup> 

## AFFILIATIONS

<sup>1</sup>School of Mathematics, South China University of Technology, Guangzhou, China

<sup>2</sup>Neuroscience Institute and Department of Mathematics & Statistics, Georgia State University, 100 Piedmont Ave., Atlanta, Georgia 30303, USA

<sup>a)</sup>Electronic mail: [qixixi954@gmail.com](mailto:qixixi954@gmail.com)

<sup>b)</sup>Electronic mail: [jiezang97@gmail.com](mailto:jiezang97@gmail.com)

<sup>c)</sup>Electronic mail: [mashqliu@scut.edu.cn](mailto:mashqliu@scut.edu.cn)

<sup>d)</sup>Author to whom correspondence should be addressed: [ashilnikov@gsu.edu](mailto:ashilnikov@gsu.edu)

## ABSTRACT

In neuroscience, delayed synaptic activity plays a pivotal and pervasive role in influencing synchronization, oscillation, and information-processing properties of neural networks. In small rhythm-generating networks, such as central pattern generators (CPGs), time-delays may regulate and determine the stability and variability of rhythmic activity, enabling organisms to adapt to environmental changes, and coordinate diverse locomotion patterns in both function and dysfunction. Here, we examine the dynamics of a three-cell CPG model in which time-delays are introduced into reciprocally inhibitory synapses between constituent neurons. We employ computational analysis to investigate the multiplicity and robustness of various rhythms observed in such multi-modal neural networks. Our approach involves deriving exhaustive two-dimensional Poincaré return maps for phase-lags between constituent neurons, where stable fixed points and invariant curves correspond to various phase-locked and phase-slipping/jitter rhythms. These rhythms emerge and disappear through various local (saddle-node, torus) and non-local (homoclinic) bifurcations, highlighting the multi-functionality (modality) observed in such small neural networks with fast inhibitory synapses.

Published under an exclusive license by AIP Publishing. <https://doi.org/10.1063/5.0233640>

Time-delays are crucial for synergistically regulating rhythms and can affect the stability and variability of small rhythm-generating neural networks, such as central pattern generators (CPGs). They influence the timing of signaling between neurons and can determine the types and outcomes of rhythmic activity in a CPG under various environmental conditions. With varying time-delays, the CPG can exhibit either multi-stability or mono-stability in its kinetic behaviors, including diverse bifurcation phenomena and changes in rhythmic patterns. Even in simple biological neural network models, multistable bursting rhythms can arise due to the introduction of time-delays. Advanced parallel computing techniques are employed to derive and parametrically continue a computational family of Poincaré return maps for phase-lags between three constituent neurons. The attractors of these maps, such as stable fixed points and invariant curves, directly influence and determine oscillatory outcomes in both biologically plausible

and phenomenological models of rhythmic neural networks. With this computational approach generating large and accurate datasets, we can thoroughly explore how time-delays dictate which stable rhythmic patterns can coexist, emerge, or vanish, specifically due to underlying bifurcation mechanisms. Subject to intrinsic mechanisms, these seemingly simple three-cell networks can produce a rich variety of multistable rhythmic states, including phase-locked burst pacemakers, traveling-wave or peristaltic patterns, and even chimeras in which one cell repeatedly phase-slips relative to the other two, which remain phase-locked over time. Additionally, more unusual behaviors may occur, such as robust synchronous oscillations of all three cells and “phase jitter” (small phasic oscillations) in bursting rhythms. We elucidate the detailed transition mechanisms between these rhythms, including saddle-node, various pitch-fork, secondary Andronov–Hopf, and torus bifurcations, along with heteroclinic connections.

## I. INTRODUCTION

Central pattern generators (CPGs)<sup>1–12</sup> are small neural networks composed of coupled neurons that autonomously generate and regulate various rhythmic motor activities in animals, including heartbeat, respiration, mastication, and locomotion. Though structurally simple, CPGs exhibit significant complexity. They can produce stable oscillations through endogenous burst generators or network-level mechanisms. A prime example is the lobster pyloric CPG, which rhythmically controls the contraction and relaxation of stomach muscles. Typically, CPGs are composed of fundamental units like the half-center oscillator (HCO), consisting of two symmetrically arranged neurons that inhibit each other, resulting in alternating anti-phase bursting patterns.<sup>13,14</sup> Current research focuses on the rhythmic dynamics, transitions, and bifurcations in three-cell neural networks formed by interconnected HCO circuits with *delayed* and fast inhibitory synapses. Various three-cell biological circuits have been previously identified as fundamental building blocks for larger neural networks regulating various types of locomotion.<sup>15–19</sup>

Neuronal activity is a complex, collaborative process involving interactions and coupling relationships among numerous neurons. This collaboration is essential for executing various operational tasks within specific regions of the nervous system. Coupling relationships encompass both electrical signal transmission and chemical signal transfer at synapses. Due to the speed of nerve conduction, synaptic transmission time, and the time required for neuronal information processing, inevitable delays occur in signal transmission between constituent neurons.<sup>20–28</sup> These delays play a crucial role in the dynamic behavior and function of the nervous system, particularly in central pattern generators (CPGs). The presence of delays may induce changes in network rhythms and transitions between them in response to perturbations. For example, in respiratory control, CPGs must switch between different breathing patterns, such as quiet and deep breathing.<sup>29,30</sup> This switching process relies on precise delay regulation to ensure that the rhythm and intensity of breathing adapt to the body's needs.

Concerning neural oscillatory networks with time-delayed coupling, it was suggested in Refs. 31 and 32 that time-delays may enhance neural synchronization. Furthermore, as was found in Refs. 33 and 34 that the length of time-delay may have significantly different effects on synchronization. Additionally, delays can contribute to the emergence of multistability.<sup>35–37</sup> For instance, in gait control, CPGs facilitate transitions between distinct locomotion patterns, such as walking, trotting, and running, each corresponding to a stable rhythmic state.<sup>38,39</sup> Adjusting delays enables smooth transitions between these stable states, allowing for complex movement patterns. Thus, understanding the mechanisms and roles of delays is essential for uncovering the fundamental principles of CPG function and advancing neuro-engineering technologies, for example, bio-inspired robotics.

## II. METHODS

In this study, we use a generalized FitzHugh–Nagumo (gFN) model proposed in Refs. 40–43 to construct a family of delayed three-cell networks. More specifically, the two-dimensional gFN model captures some key features of typical Hodgkin–Huxley

(HH)-type square-wave bursters. This model emphasizes the essential characteristics of rhythm-generating circuits, enabling the stable generation of required dynamics without relying on specific neuronal and synaptic models. The simplicity of the gFN equations makes them particularly suitable for computational studies, especially those involving GPU-based exploration of parameters and initial conditions. We investigate how time-delays influence the generation and stability of various rhythms, including phase-locked states, periodic phase slips, and chimera-like behaviors. By modulating these delays, different neural activity patterns emerge, revealing the underlying mechanisms of CPG function across various physiological states. A key feature of multifunctional CPGs is their ability to generate multiple rhythmic outcomes within the same circuitry and transition between these rhythms.<sup>19,44–47</sup> Mathematical modeling and computational simulations serve as powerful tools for exploring the dynamics of small rhythmic neural networks, especially multi-modal or multi-functional ones.

The technique introduced in Ref. 44 has been effectively used to detect nonlocal bifurcations of bursting polyrhythms in small networks of weakly coupled neurons.<sup>43,44,47–53</sup> While a previous study<sup>52</sup> proposed a simpler neural network for stability analysis, and recent work<sup>54</sup> introduced a slow synapse model with high filtering efficiency and short time-delays, the effects of such delays in synaptic connections, both inhibitory and excitatory, in such neural networks remain yet to be fully explored. This paper addresses this gap by thoroughly investigating three-cell neural circuits with delayed inhibitory synapses.

Fitzhugh–Nagumo-like cells in biological sciences, also known historically and chronologically as generic relaxation oscillators in physics, provide a mathematical generalization of Hodgkin–Huxley-type models, capturing common dynamical features observed in biological neurons. The generalized Fitzhugh–Nagumo (gFN) model<sup>43</sup> used here incorporates additional dynamical and temporal features to more realistically replicate the behavior of biological bursters, both in isolation and under perturbations. Using this gFN neuron model, we investigate a family of several three-cell networks, described by the following coupled ODE system:

$$\dot{V}_i = V_i - V_i^3 - h_i + I_{app} + \sum_{j \neq i} G_{ji}(V_j, V_i), \quad (1)$$

$$\dot{h}_i = \epsilon \left[ \frac{1}{1 + e^{-k(V_i - V_0)}} - h_i \right], \quad i, j = 1, 2, 3. \quad (2)$$

Here, the  $i_{th}$  neuron's state is described by its fast membrane voltage  $V$  and a slow recovery or gating variable  $h$  (like in the Hodgkin–Huxley formalism);  $\epsilon$  is the inverse of a time constant that regulates the slow dynamics in the gFN neuron ( $0 < \epsilon < 1$ ); the control parameter  $I_{app}$  is an applied current, which is set to  $I_{app} = 0.4$  for all three neurons (unless otherwise specified as in the caption to Fig. 1). Constants  $V_0$  and  $k$  determine and shape the relative positions and shapes of the cubic and sigmoidal nullclines given by  $\dot{V} = 0$  and  $\dot{h} = 0$ , respectively. The default values of the parameters are  $k = 10$ ,  $\epsilon = 0.3$ , and  $V_0 = 0$ , which is also the level of the synaptic threshold  $V_{th}$  in Eq. (3). Driving or presynaptic neurons are active as long as their voltage  $V_i > V_{th} = 0$ : they are assumed to slow down

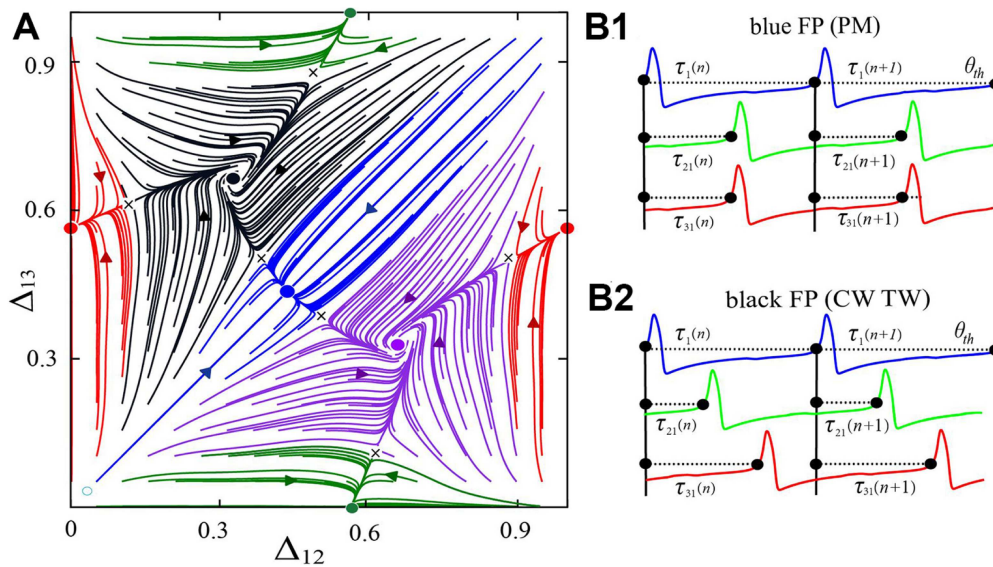


**FIG. 1.** (a) Symmetric Poincaré return map for the phase-lags,  $\Delta_{12}$  and  $\Delta_{13}$ , between the neurons is represented on unit square and features six fixed points (FPs): one repeller at  $(0, 0)$  labeled with (light blue)  $\circ$ , five attractors labeled with blue, red, and green dots  $\bullet$ , located near the default values  $(\Delta_{12}, \Delta_{13}) = (1/2, 1/2), (0, 1/2), (1/2, 0)$  referred to as *pacemakers* (PM), along with black and purple dots (CW) and counter-clockwise (CCW) *traveling wave* (TW) FPs situated near  $(1/3, 2/3)$  and  $(2/3, 1/3)$ , respectively. The black crosses  $\times$  represent saddles, whose separatrices partition the attraction basins (with matching colors) of the stable FPs, while arrows represent the directions of the forward phase trajectories of the map. (b) Phase-lags,  $\tau_1^{(n)}$  and  $\tau_{31}^{(n)}$  are defined as the delays between upstrokes in the voltage traces of the reference blue cell 1 and the following green cell 2 and red cell 3, normalized over the network period. (b1) The phase-locked PM rhythm and (b2) the CC TW rhythm corresponding to the stable black and blue FPs of the map in panel (a). Parameters:  $I_{app} = 0.419$  and  $g_{ji} = 0.0015$ .

or inhibit the driven or postsynaptic neurons by the fast, unidirectional synapses described by the fast threshold modulation (FTM) given by

$$G_{ji}(V_j, V_i) = g_{ji}(V_{rev} - V_i)\Gamma(V_j), \quad (3)$$

$$\Gamma(V_j) = \frac{1}{1 + e^{-100(V_j(t-D) - V_{th})}},$$

without or with some varying time-delay regulated by the bifurcation parameter  $D$ . The FTM formalism provides a clear distinction between active “on” and driven “off” states of a neuron. The coupling function  $\Gamma(V_j) = 1$  when the voltage  $V_j$  exceeds the synaptic threshold  $V_{th} = 0$ , and  $\Gamma(V_j) = 0$  if  $V_j < V_{th}$ . The coupling strength is controlled by the maximal conductance  $g_{ji}$  with its default value is 0.001, unless otherwise specified, to ensure weak coupling in the network. The synapse can be inhibitory or excitatory depending on the level of the reversal potential  $V_{rev}$ : if  $V_{rev} < V_i$  always, say,  $-1.5$ , it is inhibitory; elevating the level to  $+1.5$  makes the synapse excitatory.

Time-delays are an inherent characteristic of neural signal transmission in biological systems. Their inclusion in CPG models is essential for accurately simulating biological signal propagation and enhancing the models’ biological plausibility. Specifically, when the time-delay equals  $kT$  (where  $k$  is an integer and  $T$  is the network period), the system’s phase relationship remains unaffected, mirroring the behavior observed without time-delays. However, time-delays that are not integer multiples of period  $T$  can significantly

alter the phase relationship, potentially leading to phase misalignment and other complex dynamic behaviors. With this in mind, we introduce synaptic time-delays into the three-cell neural network as follows:

$$D = \alpha \cdot T, \quad (4)$$

where  $0 \leq \alpha \leq 1$  is a factor scaling down the network period  $T$  remaining around 3.63 (in some abstract time units), provided the coupling remains weak.

In what follows we will demonstrate that these three-cell gFN networks can exhibit a variety of stable phase-locked rhythms, including traveling waves, characterized by sequential cell firing, and pacemakers, where one cell effectively inhibits the other two and fires in anti-phase. The symmetric connections within the network lead to the coexistence of multiple rhythms, a consequence of the cyclic arrangement of the cells. We analyze the stability of these cyclic rhythms using the Poincaré return map for phase-lags between the constituent oscillatory neurons. Specifically, we define the phase-lag between cells as the difference in time between their burst initiations, identified by a threshold voltage crossing from below.

To analyze bursting and rhythmic spiking in central pattern generator (CPG) networks, we employ an oscillatory network computational toolkit. This toolkit simplifies the analysis by reducing it to a bifurcation analysis of phase-lags between oscillatory neurons, performed using corresponding Poincaré return maps. The

phase space structure of these maps provides a comprehensive characterization of the CPG network's functional properties. Because CPG-generated rhythms [represented by the coupled gFN system (3)] are recurrent, we can define Poincaré return maps based on the phase-lags between spike/burst onsets of the constituent neurons.

To examine the stability of different recurrent rhythms generated in a network, we utilize the Poincaré return map method. Initially, we introduce the computational concept and define the phase-lags between the constituent cells, which are determined at specific times when the cells crossed the threshold voltage from below, indicating the start of a burst. The phase-lag of a cell is then defined as the delay in its burst initiation relative to that of the reference cell 1, normalized over the bursting period. We define the relative  $n$ th phase-lags,  $\Delta_{12}^{(n)}$  and  $\Delta_{13}^{(n)}$  of cells 2 and 3, respectively, as follows:

$$\Delta_{12}^{(n)} = \frac{\tau_2^{(n)} - \tau_1^{(n)}}{\tau_1^{(n)} - \tau_1^{(n-1)}}, \quad \Delta_{13}^{(n)} = \frac{\tau_3^{(n)} - \tau_1^{(n)}}{\tau_1^{(n)} - \tau_1^{(n-1)}}, \quad (5)$$

where  $\tau_j^{(n)}$ , ( $j = 2, 3$ ) denotes the time at which the  $j$ th cell reaches the threshold voltage,  $\theta_{th} = 0$ , from below at the  $n$ th bursting cycle, see Figs. 1(b1) and 1(b2).

Now, we define and examine how the structure of the Poincaré return map  $\Pi : P_n \rightarrow P_{n+1}$  (on mod 1) of phase points  $P_n = (\Delta_{12}^{(n)}, \Delta_{13}^{(n)})$  in the forward trajectory  $\{\Delta_{12}^{(n)}, \Delta_{13}^{(n)}\}$  depends on the time-delay  $\Delta_{1j}^{(n)}$  ( $j = 2, 3$ ) in the burst initiation between the neurons of the network.

The trajectories may converge to stable fixed points, whose coordinates in the map correspond to the rhythms with specific locked phase-lags, or converge to stable invariant circles on the torus (the unit square), which correspond to distinct rhythmic patterns characterized by periodically varying phase-lags. The presence of single or multiple attractors in the corresponding 2D return map is a *de facto* proof that the given neural network is either a dedicated or a multi-functional/modal one.

The 2D return map of phase-lags,  $\Pi : P_n \rightarrow P_{n+1}$ , can be represented in the following formal form:

$$\begin{aligned} \Delta_{12}^{(n+1)} &= \Delta_{12}^{(n)} + \mu_1 f_1 \left( \Delta_{12}^{(n)}, \Delta_{13}^{(n)} \right), \\ \Delta_{13}^{(n+1)} &= \Delta_{13}^{(n)} + \mu_2 f_2 \left( \Delta_{12}^{(n)}, \Delta_{13}^{(n)} \right), \end{aligned} \quad (6)$$

where  $\mu_i$  represents the coupling strength and  $f_{1,2}$  are some undetermined coupling functions. Their zeros  $f_1 = f_2 = 0$  are the fixed points of the map  $\Delta_{1j}^{(n+1)} = \Delta_{1j}^{(n)}$ . Similar to the phase reset curves, these functions can be graphically evaluated from the simulated return maps  $\{\Delta_{12}^{(n)}, \Delta_{13}^{(n)}\}$  presented in this study.

Poincaré return maps serve as effective “blueprints” of network dynamics and the stability of rhythmic activity and have become a valuable tool in computational neuroscience. These maps are typically constructed from voltage traces by identifying successive voltage maxima or minima or by analyzing interspike intervals. Using  $f_i$  as a quantile  $\partial F / \partial \varphi_{ij}$ , one can possibly reconstruct effective “phase potentials” or coupling functions  $F(\Delta_{12}, \Delta_{13}) = C$  that unambiguously determine the dynamics of the network. This allows for the

identification of its critical points, which correspond to the attractors, repellers, and saddles within the atlas. Furthermore, scaling  $f_i$  enables the prediction of bifurcations caused by various perturbations including delays, thereby forecasting the resultant changes in the overall rhythmic outcome of the network.

A forward trajectory  $\{\Delta_{12}^{(n)}, \Delta_{13}^{(n)}\}$  of the map runs on a 2D torus, which, when flattened, is represented by a unit square. Phase-lag values such as 0 (or 1 in mod 1) and 0.5 signify in-phase and anti-phase, respectively, relationship between the reference cell 1 and two others.

In what follows, we will examine the evolution of the Poincaré return maps, such as in Fig. 1(a) and the structure of its trajectories originating off a dense population (on a  $30 \times 30$  grid) of initial phase-lags  $\Delta_{12}$  and  $\Delta_{13}$ , and hence discuss indirectly properties of the corresponding three-cell networks. By computing long sequences of the circuit's firing activity and analyzing the resulting phase-lag iterates, the latter ones eventually settle into an attractor, which may be a fixed point [with fixed coordinates  $\Delta_{12}^{(*)}$  and  $\Delta_{13}^{(*)}$  in Eq. (5)] in the 2D return map; its coordinates correspond to a stable rhythmic outcome with the same phased-locked lags. All phase trajectories that converge to the same fixed point are colored similarly, thus highlighting its basin of attraction in the map. Smaller/larger basins are associated with less/more observable rhythms generated by the network in question.

For a start, let us focus on the map presented in Fig. 1(a). This symmetric map for the homogenous three-cell network with no delay in synapses coupling the gFN-neurons at  $I_{ext} = 0.4$  shows five, stable FPs, whose color-mapped attraction basins are separated by stable sets (separatrices) of the six saddles along with a repelling FP near the origin. Notice that the total number of such structurally stable FPs on the 2D torus is always even, which allows all of them to annihilate in pairs through saddle-node bifurcations. The coordinates of the stable FPs are indeed the phase-lags locked in the voltage traces of the neurons. Specifically, due to the permutation symmetry, there are three, the so-called pacemaker (PM) rhythm where one cell regardless of its color or index bursts in anti-phase with the other two ones in sync; for example, the red FP with the coordinates  $(0, \frac{1}{2})$ , or equivalently  $(1, 1/2)$ , as the Poincaré return map for the phase-lags  $\Delta_{12}$  and  $\Delta_{13}$  is defined on mod 1. The other two PMs are color-mapped in green and blue as long as their coordinates remain close to  $(1/2, 0)$  and  $(1/2, 1/2)$ , correspondingly. The other two stable fixed points located at  $(1/3, 2/3)$  and  $(2/3, 1/3)$  in the middle of the unit square correspond, respectively, to the sequential clockwise ( $1 \rightarrow 2 \rightarrow 3$ ) (CW) and counter-clockwise ( $1 \rightarrow 3 \rightarrow 2$ ) traveling waves (CCW TWs) or peristaltic rhythms stably produced by the network. Note that if either one becomes unstable, say, for example, through a secondary torus bifurcation, the corresponding rhythm still exists but remains unstable or non-observable in the network. Whenever a stable fixed point (FP) is displaced from its original location by a delay or other synaptic perturbations, we use a different color for its basin of attraction to distinguish it from other stable and established FPs (see Sec. III).

To conclude this section, we note that trajectories of ODE system (1) and (2) are numerically integrated using a fourth-order Runge-Kutta method with a constant step size. The voltage and phase-lag trajectories, initialized under various conditions, are

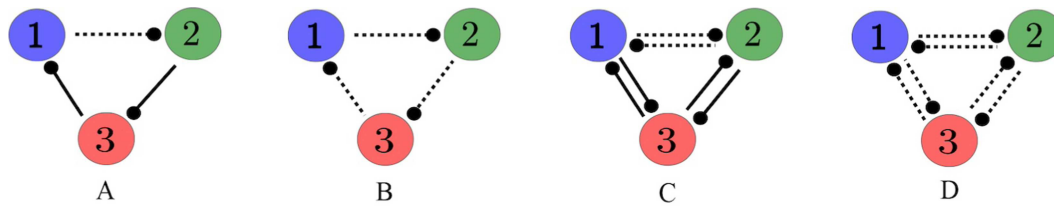


**FIG. 2.** Four key network configurations with inhibitory delayed synapses. (a) Unidirectional clockwise motif (CC) with a single delayed synapse connecting cell 1 to cell 2. (b) Unidirectional CC motif with all three delayed synapses. (c) Bidirectional motif with delayed synapses between cells 1 and 2. (d) Bidirectionally homogenous motif with all delayed inhibitory synapses. The addition of time-delays is indicated by dashed lines in the accompanying diagram.

computed in parallel on a Tesla K40 GPU utilizing CUDA, while the visualizations are generated in Python. The GPU parallelization lets one obtain such scans in seconds. The constructed phase sequences generated by the network change as time-delay is introduced and varied via the parameter  $\alpha$ . This method enables the determination of the basins of attraction for coexisting attractors and reveals the bifurcations through which fixed points emerge, vanish, or lose their stability. These crucial details would be less evident from an analysis of the voltage traces alone.

### III. RESULTS

In the following analysis, we show how the inhibitory three-cell network, by leveraging time-delays, generates several stable rhythmic patterns by alternating the active and inactive states of its constituent cells. Our analysis focuses on weakly coupled networks to maintain the visual continuity of the Poincaré return map for the phase-lags between weakly coupled neurons. The chosen sigmoidal shape of the slow  $h$ -nullcline enables the system to exploit the bottleneck effect associated with the saddle-node bifurcation, resulting in a diverse range of rhythmic behaviors.

Below, we will present an in-depth bifurcation analysis on several vital motifs of the three-cell network discussed above:

- (1) Unidirectionally clockwise-connected (CW) motif with a single synapse delaying the cell 2, see Fig. 2(a).
- (2) Unidirectionally clockwise (CW) motif with delayed synapses, see Fig. 2(b).
- (3) Bidirectionally connected motif with a delayed pair-wise synapse with two equally delayed synapses between cell 1 and cell 2, see Fig. 2(c).
- (4) Bidirectionally symmetric motif with all six equally delayed synapses, see Fig. 2(d).

The introduction and variation of synaptic delays facilitate the exploration of complex neural network dynamics, elucidating the underlying mechanisms responsible for their evolving repertoire and properties.

#### A. Clockwise motif with a single delayed synapse

Here, we focus on varying the length of time-delay by changing the  $\alpha$ -parameter in the unidirectional CW motif shown in Fig. 2(a) where the cell 1 is coupled by a delayed inhibitory synapse with the following cell 2. Note that whatever findings are true for this

motif are also applicable to other such three-cell networks with connections permuted symmetrically. The map in Fig. 3 with a single purple FP around  $(2/3, 1/3)$  demonstrates that the CCW TW rhythm is the only one observed and generated by the unidirectional CW motif with no delays. The occurrence of this sequential CW TW cycle ( $1 \rightarrow 2 \rightarrow 3$ ) implies that the activity of each following neuron is only affected by the preceding one, thus resulting in establishing a stable phase-locked relationship from the consistent cyclical inhibition. Note that this result is somewhat counter-intuitive that the given CW three-cell motif produces the only stable CCW rhythm. This result reinforces again and further demonstrates that connectivity alone is insufficient to predict network function without a thorough understanding of the underlying mechanisms

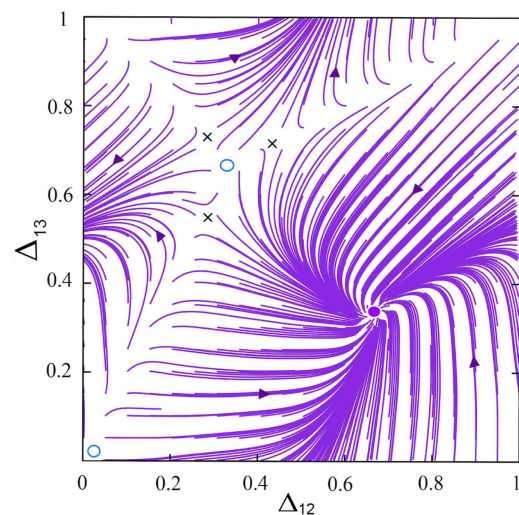


**FIG. 3.** The Poincaré return map corresponding to a unidirectional CW motif [see Figs. 2(a) and 2(b)] with no delay ( $\alpha = 0$ ). There are total six FPs in it: two repellers, at  $(0, 0)$  and  $(1/3, 2/3)$ , labeled with  $\circ$  (light blue), one attractor labeled with  $\bullet$  and three saddles labeled with  $\times$  that determine attraction basin(s) of FPs. The stable purple CCW TW at  $(2/3, 1/3)$  is the global attractor determining the mono-stable dynamics of the motif generating the only sequential ( $1 \rightarrow 3 \rightarrow 2$ ) rhythm. A cyan hollow circle ( $\circ$ ) surrounded by three saddles ( $\times$ ) nearby represents a repelling CW TW FP corresponding to a non-observable rhythm ( $1 \rightarrow 2 \rightarrow 3$ ).

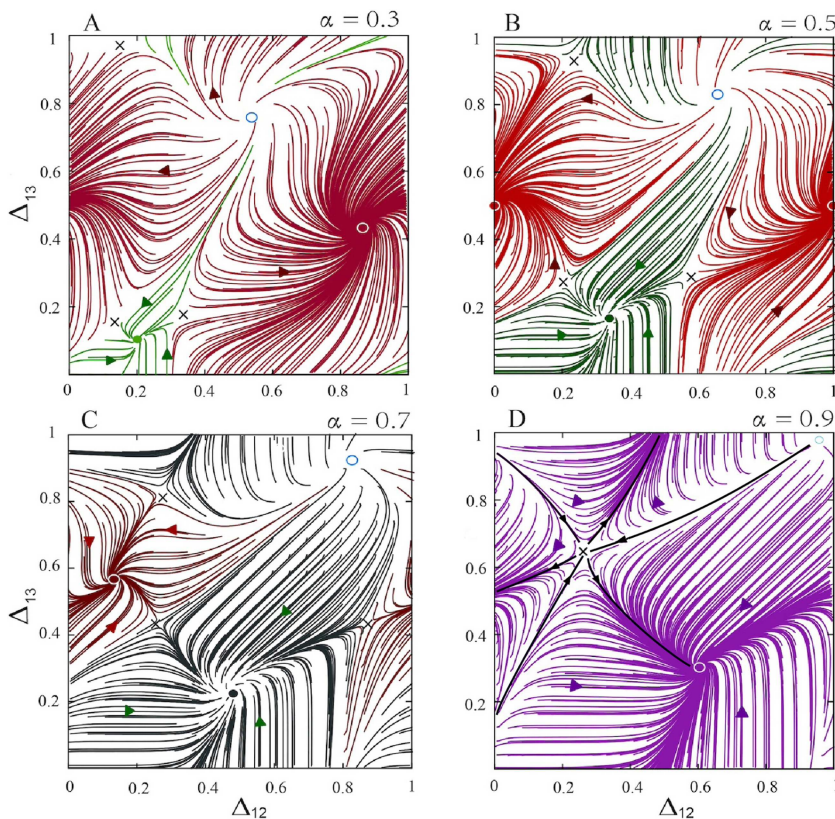


**FIG. 4.** Transformations in the 2D return map corresponding to the unidirectional CC motif in Fig. 2(a) as the time-delay is increased in the synapse connecting the blue cell 1 with the green cell 2. (a–c) The transitioning map with two attractors including a stable FP (light green) emerging through a saddle-node bifurcation occurring near the origin, and the dominant (red PM) FP, corresponding to two observable rhythms. (d) The motif becomes a mono-stable one with its phase-locked (1 → 3 → 2) rhythm corresponding to the CCW TW FP (purple) at (2/3, 1/3). The CW FP at (1/3, 2/3) is a saddle with three stable and three unstable separatrices (sets) corresponding to a co-existing but non-observable rhythm in the motif. Black crosses × represent saddles including a complex, structurally unstable one at (1/3, 2/3) with six separatrices as black lines hand-drawn and superimposed with the numerical map, while cyan hollow circles represent unstable (repelling) FPs and arrows indicate the directions of the forward phase trajectories of the map. Parameters:  $\alpha = (0.3, 0.5, 0.7, 0.9)$ .

and intrinsic nonlinear dynamics of its constituent neurons and synapses.

With a delay introduced in the single synapse one-way connecting the reference cell 1 with the cell 2, two snapshots in Figs. 4(a) and 4(b) of the Poincaré return maps for phase-lags clearly demonstrate what particular transformations the given CW motif [represented in Fig. 2(a)] undergoes as the  $\alpha$ -parameter progressively increased. The originally mono-stable motif (Fig. 3) becomes a bistable one as the map now reveals two stable coexisting FPs whose spatial positions in the unit square,  $[0, 1] \times [0, 1]$ , or the 2D phase torus, continuously change with increasing the time-delay due to  $D_{21}$ , while  $D_{23} = D_{31} = 0$ . Introducing and increasing the time-delay causes the stable dominant FP [originally purple CCW TW at (2/3, 1/3)] to move up and right from its initial position closer to (1, 1/2) in the map, see Fig. 4(a)]. Accordingly, its basin is re-colored in red as this position corresponds to the leading and dominant pacemaker—the cell 3 of the network. This red PM FP now co-exists with another stable FP around (0.2, 0.1) shown in light (fresh) green that has emerged though a simple saddle-node bifurcation. Observe how the separatrices (stable sets) of two saddles demarcate the borderlines between the attraction basins, large and small, of these coexisting FPs.

When the parameter  $\alpha_{12}$  is increased further from 0.5 through 0.9, the comparison of the return maps in Figs. 3(b) and 3(c) helps one figure out how these stable two FPs transition in the map. The red stable FP shifts further right on the torus to re-emerge

on the left of the map where it meets with a saddle and annihilate through another saddle-node bifurcation. Meanwhile, the remaining stable (now black) FP gets closer to the position near (2/3, 1/3) where it regains its original purple color corresponding to the CCW traveling rhythm of this neural motif, as in its case with no delay, with  $\alpha_{12}$ -values close +1, see Fig. 3(d). Consequently, the motif reverts to its expected monostable state, compare with the map in Fig. 3. However, there is a subtle yet principal difference in these two cases. One can see that in the former case the CW FT is a repeller, whereas in the last case it is a complex saddle with six separatrices (sets), three stable and three unstable. This structurally unstable saddle is the result of the merger of a stable or repelling FP with three nearby saddles through a pitch-fork bifurcation (with four prongs) typical for equivariant systems with the  $S_3$ -symmetry, as well as the 1:3 resonance with a period-3 orbit on a circle due to rotation through the  $2\pi/3$ -angle.<sup>55</sup> This saddle, should  $\alpha_{12}$  be brought closer +1 (or 0), will quickly decompose into the repeller and three surrounding saddles as Fig. 3 reveals.

Note that the observed transitions are mediated by the delay approaching a full period, thereby preserving the system’s phase relationship. In this process, we observed the system transition between two stable fixed points (FPs), with a corresponding shift in their locations. Therefore, the time-delay affects not only the stability of the FPs but also their spatial position, globally influencing the dynamic behavior of this three-cell motif.

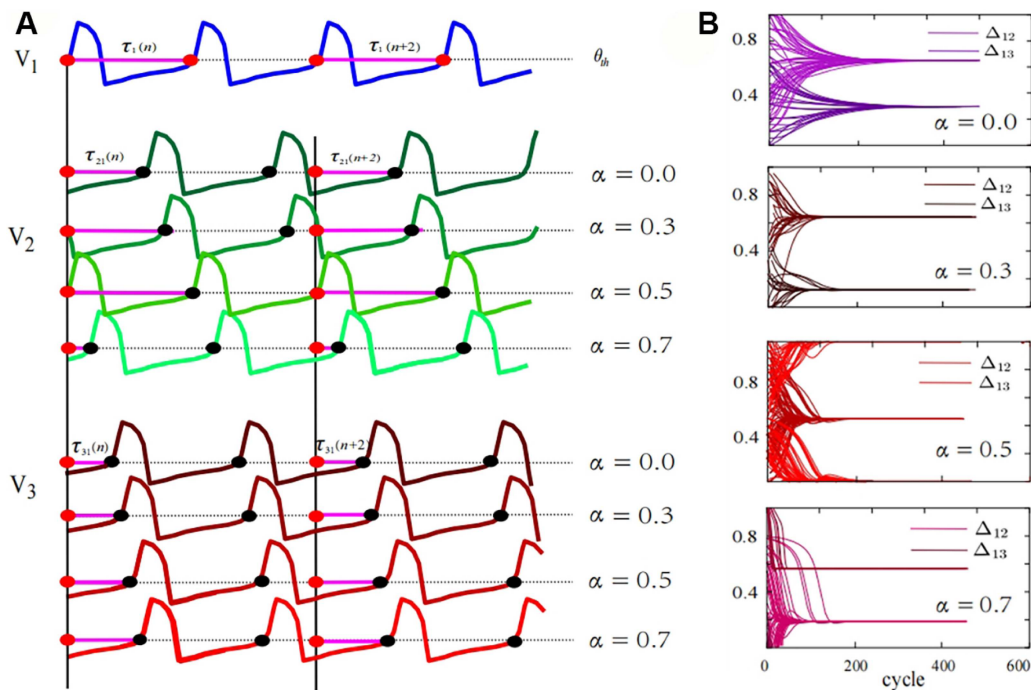


**FIG. 5.** (a) The voltage traces and (b) time progressions of phase-lags  $\Delta_{12}$  and  $\Delta_{13}$  associated with the (purple) stable FP of the return map for the CW motif with the single delayed synapse. The darker and lighter colors of the voltage traces  $V_2$  and  $V_3$  in (a) and the phase-lag progressions in (b) correspond to shorter and longer time-delays as  $\alpha$  is discretely increased from 0 through 0.7.

Figure 5 illustrates the time progressions of voltages recorded from all three neurons, as well as the corresponding phase-lag progression as the delay is varied from  $\alpha = 0$  through  $\alpha = 0.7$ . These diagrams are specifically based and reflect on the movement of the stable (purple) CCW TW FP shown in the map (Fig. 4) to provide a detailed explanation of the gradual changes of the phase-lags in the specific rhythm generated by the motif under specific time-delays. While the time series representation presented in Fig. 5(a) depicts the motif's temporal evolution prior to reaching a steady state, Fig. 5(b), illustrating the convergence of differing initial phase-lag configurations to the stable, phase-locked states, manifests a more comprehensive understanding of this mono-stable convergence phenomenon.

### B. Unidirectional CW motif with three delayed synapses

In this section, we study the dynamics of the unidirectional CW motif [depicted in Fig. 2(b)] with three equally delayed synapses. The six snapshots in Fig. 6 illustrate the evolution of the Poincaré return maps, and hence of the given motif, as delay due to the  $\alpha$ -parameter is increased.

Figure 6(a), computed with all three synapses initially delayed with  $\alpha = 0.2$ , reveals the bistability in this motif where the expected CCW TW (compare with Fig. 3 with no delay) co-exists with a stable FP (yellow) at the origin that corresponds to a fully

synchronous state, i.e.,  $\Delta_{12} = 0$  and  $\Delta_{13} = 0$ . Note that such synchronous rhythms are typically observed in small neural networks where all synapses are either electric or excitatory ones. Apparently, this and some longer delays make fast inhibitory synapses act as excitatory ones. Moreover, we can only hypothesize how this synchronous FP becomes stable as intermediate transformation stages are skipped as  $\alpha$  is gradually increased with 0 to 0.2. There is basically a single bifurcation option that lets a repeller become an attractor, which is an Andronov–Hopf bifurcation in systems with continuous time, or a secondary torus bifurcation in systems with discrete time that gives rise to the onset of a periodic orbit or an invariant curve, respectively. The former case in the given Poincaré return maps for phase-lags will be discussed in the concluding result section of the paper, as detailed as possible in a computational paper like ours. The presumed torus bifurcation, sub- or super-critical, giving rise to an IC, is also accompanied with a heteroclinic connection between all three saddles nearby through which the round IC emerges from or terminates into. Needless to add that the discrete case can be more complex as one has to take into considerations other factors, for example, a winding number on the IC that can make it resonant before its possible breakdown, and so forth.

Figure 6(b) reveals that this new yellow FP at the origin becomes nearly a global attractor of the map at a longer delay with  $\alpha = 0.3$ , after three saddles come close to block the attraction basin of the CCW TW. Recall that the given attractor corresponds to the fully synchronous rhythm in the CW motif under consideration.

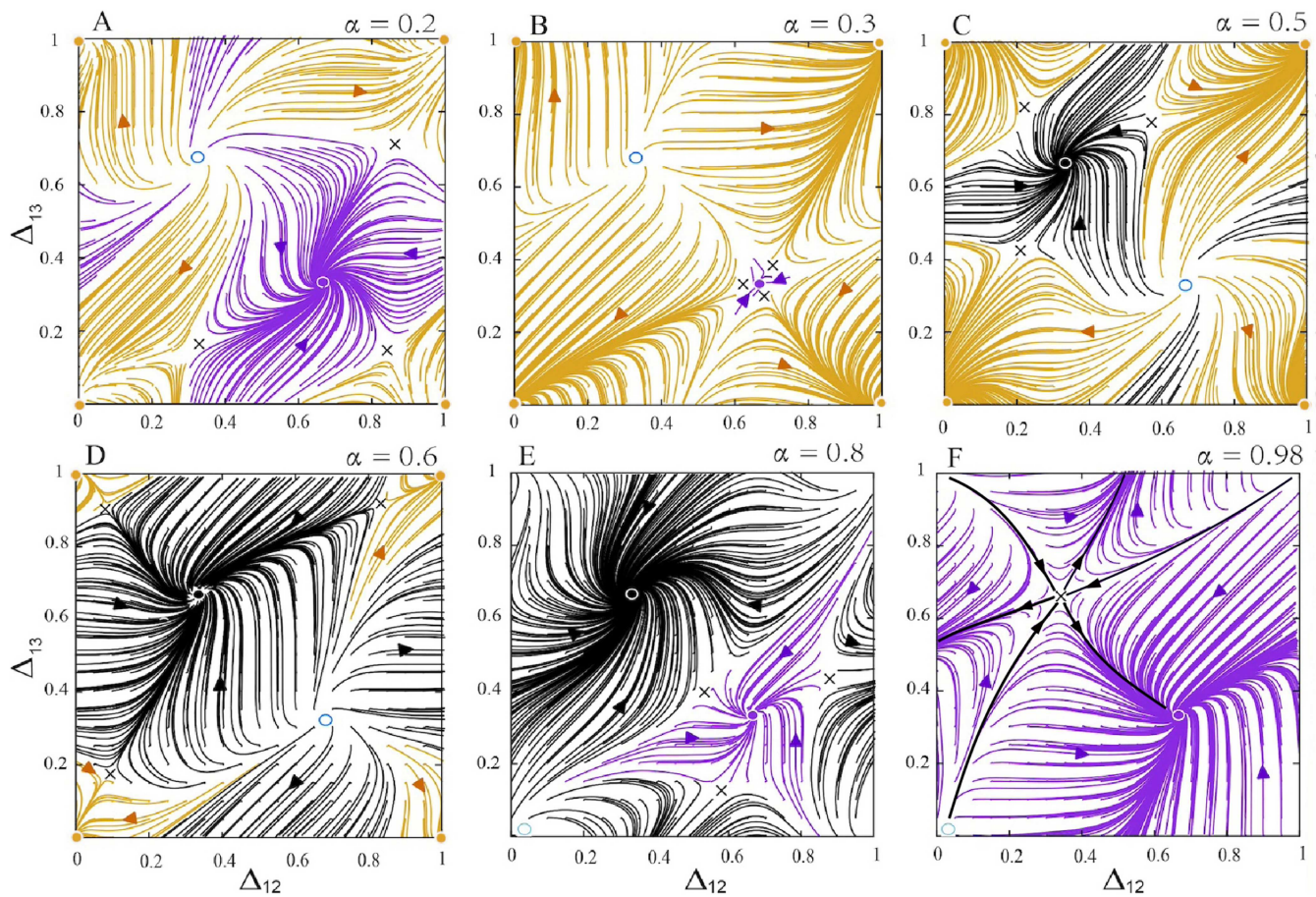


**FIG. 6.** Six snapshots of the Poincaré return maps corresponding to the unidirectional CC motif in Fig. 2(b) with all delayed synapses as the  $\alpha$ -parameter is increased. (a) The bistable map with a synchronous FP (yellow) near the origin and the CCW FP (purple). With further increasing  $\alpha$  the attraction basins of the synchronous FP and CCW TW FP become redistributed as the separating saddles move around the unit square. (b) The basin of the TW FP shrinks as three nearby saddles approach to reverse its stability. (c) The repelling [in (b)] CW FP at  $(1/3, 2/3)$  (black) becomes stable due to a reverse bifurcation. (d) Its basin expands while the basin of the synchronous (yellow) FP shrinks with a further  $\alpha$  increase after three saddles approach the latter to make it unstable. (e) The CCW FP (purple) regains its stability through a reverse bifurcation and (f) becomes the only attractor of the map and the dominating  $(1 \rightarrow 3 \rightarrow 2)$  rhythm of the motif; here, the CW FP is a complex, structurally unstable saddle with six separatrices and black lines hand-drawn and superimposed with the computed map. Black crosses represent saddles, cyan hollow circles represent unstable FPs, and arrows indicate the directions of the phase trajectories of the maps. Parameters:  $\alpha = (0.2, 0.3, 0.5, 0.7, 0.8, 0.98)$ .

As the time-day becomes longer in Fig. 6(c), the purple CCW TW becomes a repeller, whereas oppositely the repelling CW TW FP becomes stable through a two-step transformation: first a heteroclinic triangle-shape connection between the saddles followed by a secondary torus bifurcation. Increasing the time-delay in all three inhibitory synapses of the motif causes the saddles move closer to the yellow FP to first bound its basin in Fig. 6(d) and second make it a repeller in Fig. 6(d). Meanwhile, the reverse bifurcation sequence brings the CCW TW attractor at  $(2/3, 1/3)$  back to the map. When the delay becomes larger, the attraction domain of the black CW TW FP starts to shrink, and at some critical  $\alpha$ -value it becomes unstable so that the motif returns to its original monostable state. Figure 6(f) depicts the very beginning of the stability loss of the CW FP where it becomes a complex saddle with six separatrices at the moment

of its merger with three saddles nearby. Increasing  $\alpha$  from 0.98 to 1.0 restores the status quo of this monostable unidirectional CW motif, which as we have seen can be bistable when its synapses are delayed within certain margins. Here, the motif can switch between synchronous and traveling wave rhythms with perturbations applied to its targeted neuron(s).

### C. Bidirectional motif with two synapses equally delayed

In such a motif, see its circuitry in Fig. 2(c), the delay is introduced and regulated in two reciprocally inhibitory synapses between the cell 1 and cell 2. It is evident that this should eventually break



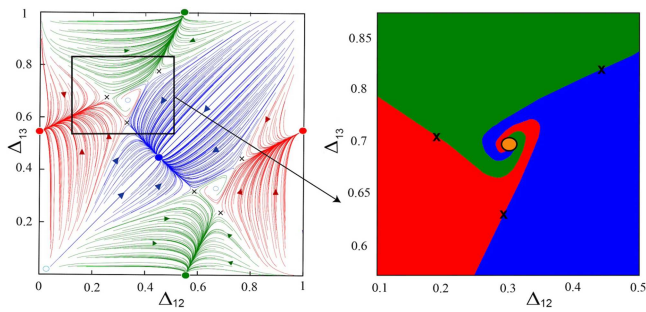


**FIG. 7.** (a) The symmetric Poincaré return map with a zero delay ( $\alpha = 0$ ) and (b) its magnified fragment depicted near the repelling CW FP; borderlines between the attraction basins are determined by the incoming or stable separatrices (invariant sets) of the nearby three saddles labeled by  $\times$ .

down the  $S_3$ -symmetry of the network, which is *de facto* a prerequisite for the existence of the CW and CCW TW rhythms, and of the PM rhythms led by the selected cells.

Figure 7 depicts the return map for the phase-lags on the bidirectional motif with no delays in its synapses. Here, the CW and CCW rhythms cannot be observed as the corresponding FPs in the map are unstable foci as one can observe from the magnified section of the figure. It is easy to see from the map that such a symmetric motif can only generate three PM rhythms with the same probability. Note that the map illustrates what is known as dynamical uncertainty: starting from an initial phase difference close to either unstable FP, the trajectory will spiral away heading toward one of the stable PM FPs. Same is true for solutions close to the synchronous state as well. This dynamical uncertainty has a significant impact on the rhythmogenesis in such a motif: the traveling rhythms are no longer observable, and after some transient this multi-modal motif

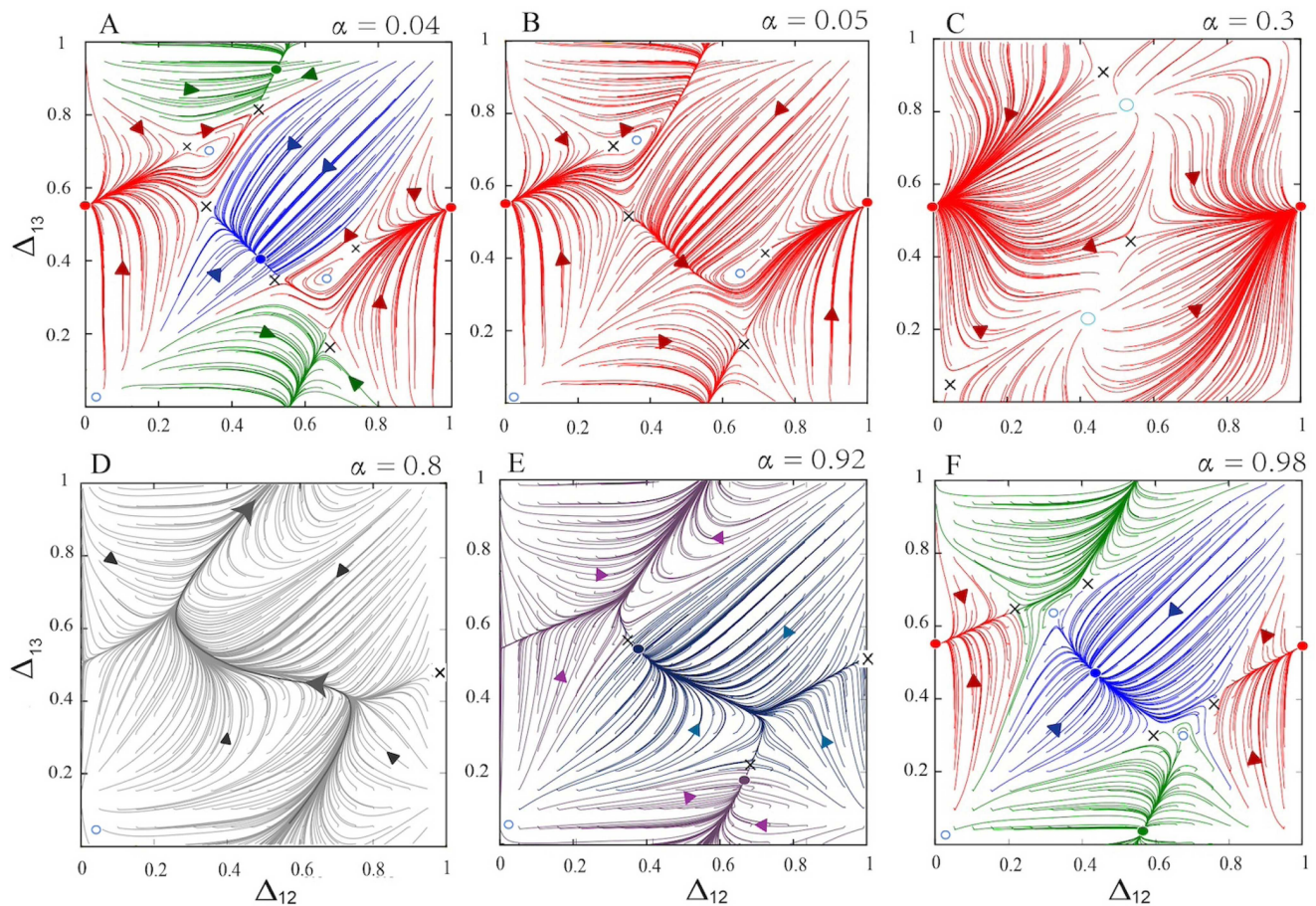


**FIG. 8.** Six snapshots of the Poincaré return maps corresponding to the bidirectional motif [Fig. 2(c)] with delayed synapses between cells 1 and 2. (a) Introducing the delay unbalances the motif and forces the green and blue FPs to vanish simultaneously through simple SN-bifurcations, leaving the map being dominated by the red PM FP in panel (b). Further  $\alpha$ -parameter increase also breaks down the CW and CCW symmetries of the motif and hence annihilates the corresponding FPs with close saddles ( $\times$ ) through SN-bifurcations in panel (c). As  $\alpha$  increases from 0.5 to 0.7, the map demonstrates mono-stability due to a single periodic attractor—a stable invariant cycle (IC in gray), emerging through a heteroclinic SN-bifurcations that wrap around the torus and corresponds to periodic phase shifting (PS) between the neurons 1 and 2. (e) The purple and blue FPs re-emerge in the map through a reverse heteroclinic SN-bifurcations and so did the red PM through a simple SN-one in panel (f) to complete the full round as  $\alpha$  is increased to its upper limits. Arrows represent the directions of the phase trajectories of the return maps. Parameters:  $\alpha = (0.04, 0.05, 0.3, 0.5, 0.8, 0.98)$ .

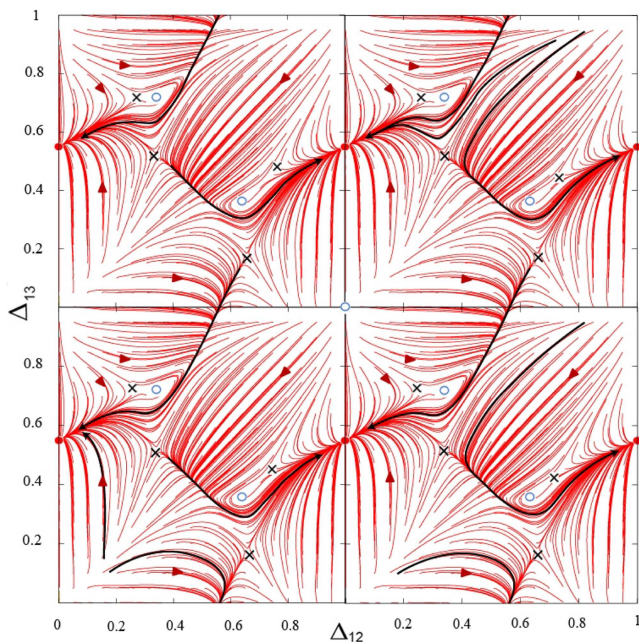


**FIG. 9.** Continued from Fig. 8(b): four identical panels are stitched together to visualize and better understand how trajectories populate and wrap around the phase torus, which is dominated by a single red PM at  $(0, 0.5)$ . The saddles, located nearby, cause two trajectories from close initial conditions to traverse different pathways (black lines hand-drawn and superimposed with the computed map) leading toward the red FP.

stabilizes into one of the three PM rhythms [see Fig. 7(b)]. External perturbations applied to targeted neurons can trigger switches between the three robust rhythms.

Figure 8 shows the evolution of the Poincaré return maps as  $\alpha$  is increased from 0.2 through 0.98. A short delay is introduced to two inhibitory synapses between the cells 1 and 2 in order to break down the  $S_3$ -symmetry of this bidirectional motif. This is documented in Figs. 8(a) and 8(b) showing that both corresponding blue and green PM FPs undergo saddle-node bifurcations that annihilate them along with two saddles. One can see from Figs. 8(b) and 8(c) that the PM rhythm led by the red cell 3 remains the only one in the repertoire of this motif, even though the TW FPs still exist in the map.

Throughout an extended parameter range  $\alpha \in [0.05, 0.7]$ , the motif's dynamics is dominated by the red PM rhythm corresponding to the stable red FP at  $(0, 1/2)$  to which all trajectories converge by following different paths (black curves) with variable converge rates, as seen in Fig. 8(b). To better understand the transient dynamics of the motif, and using the property that the map is defined on the phase torus on modulo 1, one may find useful to consider four identical panels stitched together, as done in Fig. 9, to visually inspect rather a “continuous” trajectory behavior.

Figure 8(d) illustrates a qualitative change in the motif's behavior. The previously observed rhythm with locked phases is replaced by a rhythm characterized by periodically varying, or shifting,

phases. The map here has a single attractor, which is a stable invariant curve (IC) that wraps around the phase torus, or the unit square from its bottom to the top, passes sequentially throughout the “ghosts” of the four disappeared FPs: the green PM one at  $(1/2, 0)$ , the CCW TW one at  $(2/3, 1/3)$ , the blue PM one at  $(1/2, 1/2)$ , and the CW TW FP at  $(1/2, 2/3)$  to start over. In this case, the IC formation undergoes two stages: two simultaneous SN-bifurcations through which both TW FPs are eliminated, followed by the elimination of the red FP through a homoclinic SN-bifurcation, whose stability is inherited by the IC, which corresponds to the so-called *phase slipping* rhythm. Note that besides the stable IC, the map has still two FPs: a repeller close to the origin and a saddle located at the position of the red FP near  $(0, 1/2)$  or  $(1, 1/2)$ . Should the motif be perturbed differently, both FP may merge too and vanish through another homoclinic SN-bifurcation to produce a repelling IC. We can hypothesize further with perturbations to force both ICs merge and disappear as well, so that the torus will get covered densely by a single trajectory.

Figure 8(e) validates our bifurcation scenario and shows that the IC is replaced by the heteroclinic connection between two saddle-node FPs that give rise to the two stable PM FPs located on the IC ghost. Further increasing the delay with  $\alpha = 0.98$  completes the cycle; here the map gains all three stable PM FPs, including re-emergent red one, at the fixed, pre-set locations.

#### D. Bidirectional motif with all delayed synapses

This is the final motif, presented in Fig. 2(d), with all six delayed and manipulated synapses that we analyze in this study case.

Five panels of Fig. 10 present four snapshots of the return map operating corresponding to the bidirectional motif with short time-delays due to small value of the  $\alpha$ -parameter. This symmetric motif is dominated by three PMs, coexisting with two stable (gray) ICs around repelling TW FPs that emerge simultaneously through supercritical torus bifurcations in Fig. 10(a). These two ICs represent the phenomena referred to as periodic “phase-jitter,” i.e., the phase-lags of the neurons oscillate stable around the values  $(1/3, 2/3)$  and  $2/3, 1/3$ , depending on their initial states; it is observed in various coupled systems, including neural networks<sup>49</sup> and nonlinear optics.<sup>56,57</sup> These two quasi-periodic orbits (ICs) emerge off the CW and CCW TW FPs as the zoomed Fig. 11(a) depicts. The time progression of the corresponding voltage traces and phase-lags reflect the periodical variations rather than fixed locked states, see Figs. 11(b) and 11(c). One can foresee from this figure that as the parameter is further increased, each IC becomes a one-way heteroclinic orbit connecting three nearby saddles after which it disintegrates.

Figure 10(b) reveals the further bifurcation unfolding of the return map: both stable ICs increase in size and become dominant attractors in the map after the PF bifurcations simultaneously transform the red, green, and blue PM attractors into saddles at same locations,  $(0, 1/2)$ ,  $(1/2, 0)$ , and  $(1/2, 1/2)$ , respectively. With a longer time-delay, a plain saddle-node bifurcation occurs on the bisectrix near the origin that makes it stable, see Figs. 10(b)–10(d). Its basin quickly increases in size at  $\alpha = 0.13$  after both stable ICs disintegrate when they reach the saddle FPs. A following SN-bifurcation eliminates the repeller and the saddle on the bisectrix

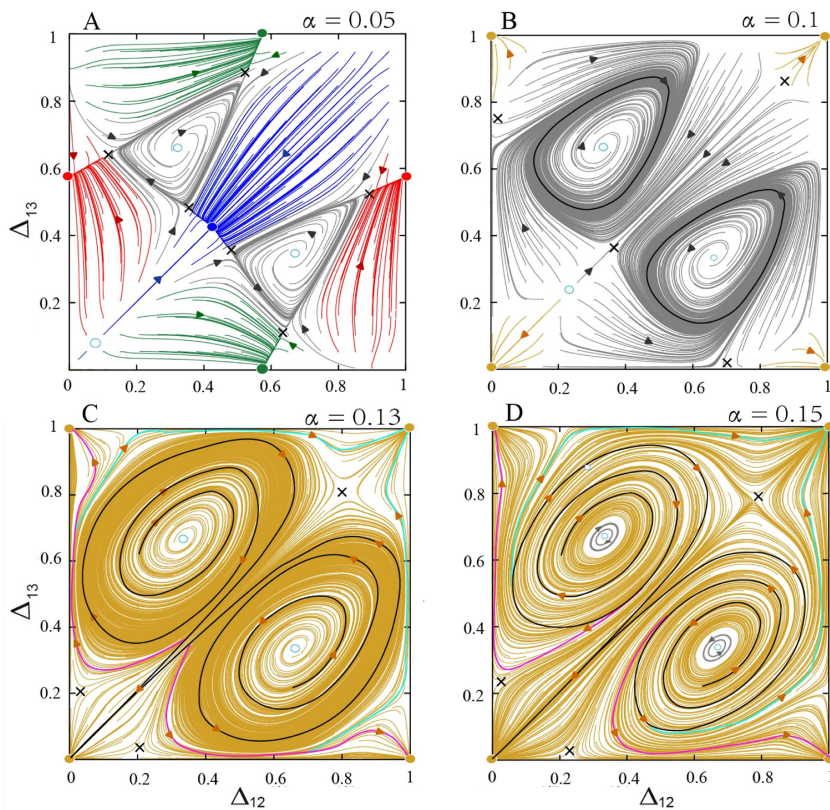


**FIG. 10.** Four snapshots of the Poincaré return map for the bidirectional motif in Fig. 2(d) illustrate its transformations as all synapses are progressively delayed within a short range [0.05, 0.15]. (a) This symmetric motif is dominated by three PMs, coexisting with two stable (gray) ICs (representing periodic phase-jitter phenomena) around repelling TW FPs that emerged through supercritical torus bifurcations. (b) As the time-delay is increased, the stable ICs become dominant after the PF bifurcations transform the red, green, and blue PM attractors into saddles at same locations,  $(0, 1/2)$ ,  $(1/2, 0)$ , and  $(1/2, 1/2)$ , respectively. With a longer time-delay, a saddle-node bifurcation occurs on the bisectrix near the origin that makes it a stable (yellow) FP. (c) Its basin quickly increases in size at  $\alpha = 0.13$  after both stable ICs disintegrate when they reach the saddle FPs. (d) Another SN-bifurcation eliminates the repeller and the saddle on the bisectrix after which the origin becomes the global attractor of the map with two more repellers and three saddles. Arrows represent the directions of phase trajectories includes special ones color-selected. Parameters:  $\alpha = (0.05, 0.1, 0.13, 0.15)$ .

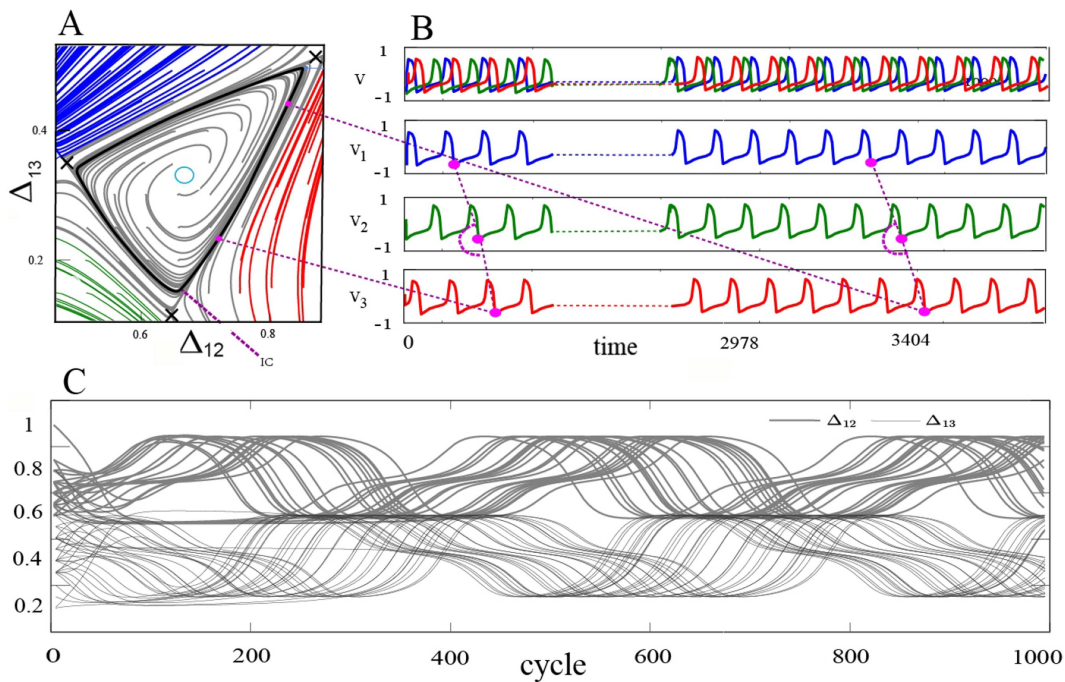


**FIG. 11.** A magnified fragment of the return map from Fig. 10(a) depicting a stable IC around the repelling CW FP at  $(\Delta_{12} = 2/3$  and  $\Delta_{13} = 1/3)$ . (b) The corresponding voltage traces and (c) the associated progressions of phase-lag jitters.

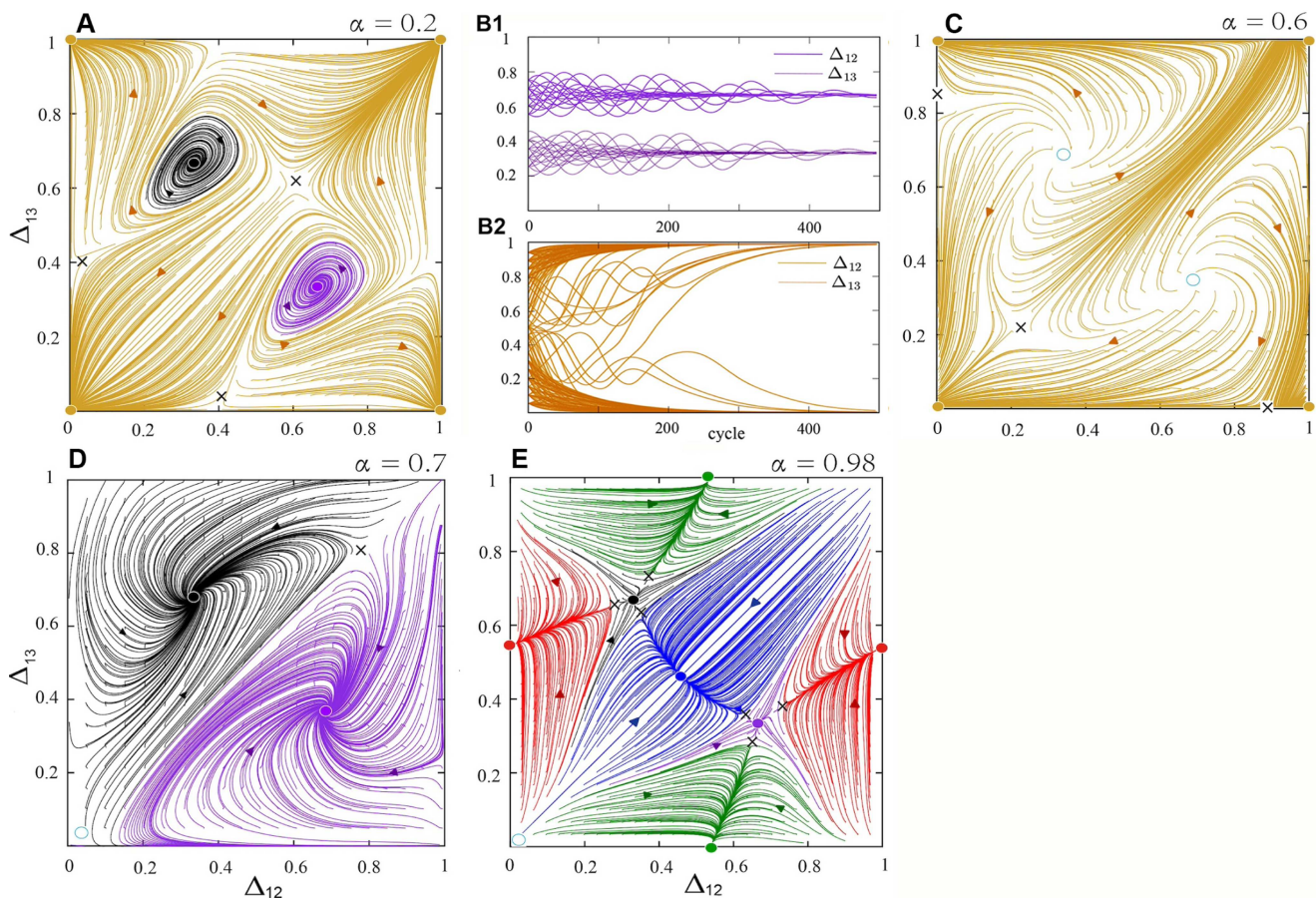
after which the origin becomes the global attractor of the map, which is *de facto* proof that the synchronous rhythm is the only one generated by this motif.

Figure 12 showcasing the return maps is an extension of Fig. 10 for the bidirectional motif with longer time-delays. We can see that the TW FPs regain, loose, and regain their stability as the  $\alpha$ -parameter is increased all the way up to 0.98, basically following the same bifurcation mechanisms described above for the bidirectional motif with short delays, which include forward and reverse torus and pitch-fork bifurcations. In between the synchronous rhythm solely determine the repertoire of the given motif. Two stable foci [black and purple at  $(\Delta_{12} = 1/3, \Delta_{13} = 2/3)$  and  $(\Delta_{12} = 2/3, \Delta_{13} = 1/3)$ , respectively] existing in the map in Fig. 12(a) disappear in Fig. 12(c) so that the yellow synchronous FP at the origin determines the existence of the only robust rhythm generated by the mono-stable neural motif. The motif becomes bistable with two TW rhythms at longer

delays [Fig. 12(d)] before it becomes penta-stable as  $\alpha$  approaches its upper limit +1.

Recall that near a heteroclinic bifurcation, particularly one yielding a stable, round invariant curve (IC), the period can become arbitrarily large (logarithmically), as is determined by the number of iterations required for phase points to traverse a saddle. Consequently, phase jitter frequency slows significantly near the heteroclinic connection. Figure 11 illustrates this phase jitter in voltage waveforms (panel b) and phase-lag oscillations (panel c).

We would like conclude this section by elaborating on the torus and heteroclinic bifurcations in the extended phase space presented in Fig. 13 that depicts the key transformation stages occurring in the map (bidirectional motif) near the TW FPs, specifically close to the CW one at  $(1/2, 2/3)$ , as the  $\alpha$ -parameter (time-delay) is varied between 0.02 and 0.2.



**FIG. 12.** For panels of the Poincaré return map corresponding to the bidirectional motif in Fig. 2(d) with all six inhibitory synapses delayed equally. (a) The motif with a short delay produces synchronous and two CW and CCW TW rhythms, corresponding, respectively, to the stable FP at the origin  $(0, 0)$  and at  $(1/3, 2/3)$  and  $(2/3, 1/3)$ . (b) The time progressions of phase-lags of the oscillatory neurons converging to the CW and CCW TWs (b1) and synchronous (yellow) state (b2) in the symmetric triple-modal motif with delay due to fixed parameter  $\alpha = 0.2$ . (c) Longer delays make both TW FPs repelling through the torus bifurcation, and the synchronous rhythm only observable. (d) The TW FPs regains stability after the origin lost it. (e) The Poincaré return map with five stable FPs for a nearly symmetric bidirectional motif. Arrows represent the directions of phase trajectories. Parameters:  $\alpha = (0.2, 0.6, 0.7, 0.98)$ .

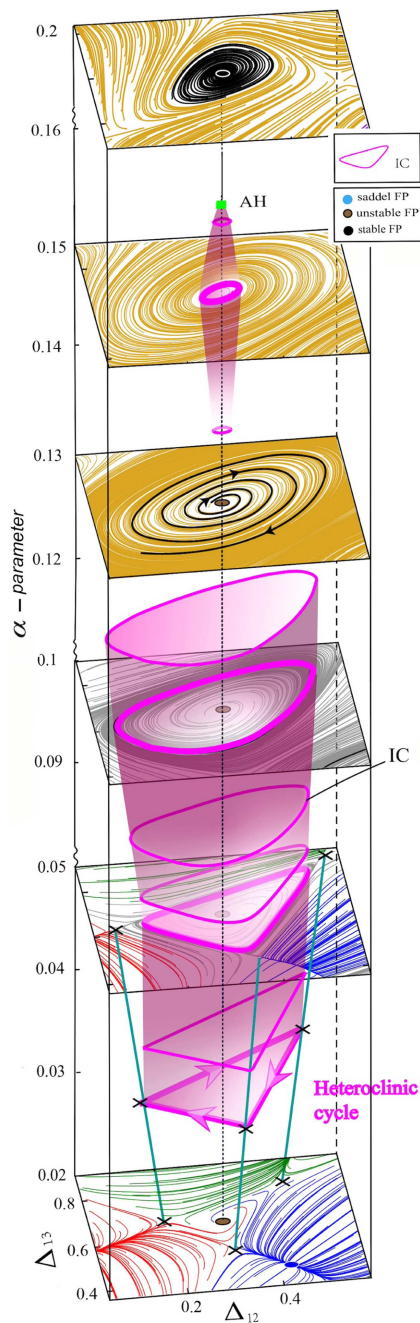


**FIG. 13.** This bifurcation diagram depicts key stages of the supercritical torus (or secondary Andronov–Hopf) bifurcation and the heteroclinic bifurcation of the fixed points (FPs) within the  $\alpha$ -extended phase space. A paraboloid-shaped surface is foliated by the stable, round invariant curve (IC) that emerges from the clockwise traveling wave fixed point (CC TW FP). This invariant curve terminates in a heteroclinic connection between three surrounding saddle points. Subsequently, the invariant curve re-emerges and collapses back into the original fixed point through two reverse bifurcations. Solid lines represent the evolution of stable FPs, while dashed lines indicate unstable FPs.

The bottom of the 3D bifurcation diagram is map where the CW FP is a repeller at  $\alpha = 0.02$ , which is surrounded by three saddles nearby. As  $\alpha$  is initially increased, the saddles form a one-way heteroclinic connection (purple curve) or cycle that gives rise to the onset of the stable round IC. As  $\alpha$  is further increased, the size of the stable IC starts increasing and next decreasing, so that it collapses into the CW FP and makes it stable at 0.2 through a super-critical torus bifurcation. Once can see a paraboloid-like surface foliated by the shrinking IC. In this diagram, the solid and dashed lines represent the coordinate parameters of the stable FP and saddle FP, respectively.

This bifurcation diagram offers deeper insights into the semi-local dynamics of the bidirectional motif, thereby providing a valuable resource for a comprehensive understanding of nonlinear interactions of the three coupled neurons. The exact location of the bifurcations can be accurately identified through a refinement process.

#### IV. CONCLUSIONS AND FUTURE DIRECTION

We conducted a case study on a three-cell neural network weakly coupled by delayed inhibitory synapses. Our goal was to demonstrate the network's capacity for diverse, often counter-intuitive, rhythmic outputs in response to time-delay variations. These dynamic properties are determined by both synaptic properties and the individual neuron states. We analyzed several key multi-modal motifs supporting both single and multiple rhythms, depending on the synaptic time-delay. We also explored potential switching mechanisms between robust rhythmic states in biological systems. Using phase-lags between neurons, we computationally generated Poincaré return maps from multiple voltage traces, providing a powerful framework for analyzing rhythmic behavior in small neural networks with diverse synapses and circuitries. The use of GPU computing enables rapid, parallel generation of these return maps in seconds.

The computational tools presented here are designed to reflect common features of electrophysiological experiments. Crucially, our approach requires only voltage recordings from the model cell, mirroring the typical constraints of experimental settings. Our analysis is based on the phase derived from this voltage, the primary measurable variable in experiments. Furthermore, analogous to experimental protocols, we control the initial phase distribution by precisely timed inhibition release of neurons relative to a designated reference neuron. Our analysis relies exclusively on qualitative geometric methods from dynamical systems theory. While we use a system of differential equations for illustrative purposes, these methods can be applied directly to experimental data, obviating the need for explicit knowledge of the underlying model equations. This approach, which analyzes phase-lag and return maps independent of the system's mathematical description, can be generalized to a wide range of complex biological and engineered systems. Examples include applications in engineering, economics, population dynamics, dynamic memory, animal decision-making,<sup>58</sup> and the development of efficient robotic locomotion.<sup>59–61</sup> These computational techniques provide a powerful means of comprehensively examining the rhythmic behavior exhibited by these networks.

Investigating rhythmic transitions necessitates manipulating the time lag of synaptic connections within different network

architectures. In biological systems, such manipulations can be achieved by altering the transmission properties of synapses, through chemical interventions or external perturbations (current pulses). These diverse network structures can generate a wide range of rhythmic behaviors, including phase-locked ruptures coupled with pacemakers or traveling waves, as well as cyclic phase-slip chimeras. Changes in network parameters can induce a variety of bifurcations, such as saddle-node, torus, and secondary Andronov–Hopf bifurcations, leading to the emergence or disappearance of rhythmic states and the gain or loss of their stability.

Our findings reveal that traveling wave dynamics are the dominant characteristic of single-connected central pattern generator (CPG) motifs. Increasing time-delays leads to transitions between distinct rhythmic patterns within the network, with traveling waves becoming increasingly prevalent at higher delay values. Significantly, this implies that the introduction of time-delay in single connections is sufficient to predict the range of rhythmic behaviors a given network can generate, even without prior knowledge of the qualitative mechanisms underlying rhythm generation, escape or release phenomena, or the quantitative strength of synaptic connections. This predictive capability is essential for designing verifiable hypotheses in neurophysiological experiments investigating diverse biological systems of coupled oscillators and CPG circuits. Finally, we note that in central pattern generators, the mutual conversion between two fixed points via a bifurcation frequently corresponds to the system transitioning from one movement pattern to another, as observed in gait transitions.

Central pattern generators (CPGs) play a crucial role in coordinating limb movements in biological systems, enabling transitions between different gaits. A clear example is the shift from walking (a slow gait) to running (a fast gait) observed in horses. This transition represents a shift between distinct stable equilibrium points corresponding to each gait. By analyzing bifurcation phenomena and constructing phase diagrams, we can gain a deeper understanding of the underlying mechanisms governing biological motion control. These insights provide critical theoretical foundations for the design and development of both bio-mechanical devices and bionic robots. Our results demonstrate that a doubly connected network, when subjected to a single time-delay, exhibits a strong tendency to remain at a single equilibrium point for extended periods. The introduction of the time-delay promotes synchronization between cell 1 and cell 2, while also facilitating the emergence of phase slips, which allow the system to transition between multiple stable points. Furthermore, in this delayed, doubly connected network, we identified heteroclinic cycles. These cycles form the basis of the “no-winner competition principle,” a mechanism that drives robust and continuous behavioral repetitions in small neuronal networks. We show that tracking invariant curves and heteroclinic cycles within the phase-lag return maps enables the prediction and detection of “hidden” bursting rhythms in the motif in question. These bifurcation phenomena provide the necessary theoretical framework for understanding the ubiquitous phenomenon of phase jitter synchronization, which has been widely reported in diverse applications across both physical and life sciences.

Several avenues for future research emerge from this work. First, incorporating time-delays into larger, modular neural networks built from smaller subunits<sup>62</sup> warrants investigation. Second,

utilizing biologically plausible Hodgkin–Huxley-type bursters as neural motifs could offer new insights into the resulting dynamical behaviors. Third, the application of Poincaré return maps could facilitate a comprehensive exploration of the full range of rhythmic patterns generated by a given network. Finally, extending these findings to more complex network architectures, including EI networks, and exploring the implications of the odd cycle rule<sup>63</sup> for determining the network’s oscillatory capacity promises to be a fruitful direction for future research.

## ACKNOWLEDGMENTS

This work was supported in parts by the GSU Brain and Behavior initiative and the NSF DMS 2407999 Award (to A.L.S.) as well as by the National Natural Science Foundation of China under Grant Nos. 11572127 and 11872183 (to S.L.).

## AUTHOR DECLARATIONS

### Conflict of Interest

The authors have no conflicts to disclose.

## Author Contributions

Xinxin Qie and Jie Zang contributed equally to this work.

**Xinxin Qie:** Data curation (lead); Formal analysis (lead); Investigation (lead); Methodology (equal); Software (equal); Writing – original draft (lead); Writing – review & editing (lead). **Jie Zang:** Conceptualization (lead); Investigation (equal); Methodology (lead); Project administration (equal); Software (lead); Supervision (equal); Validation (equal); Writing – original draft (equal). **Shenquan Liu:** Funding acquisition (lead); Project administration (supporting); Resources (lead); Supervision (supporting); Validation (supporting); Writing – review & editing (supporting). **Andrey L. Shilnikov:** Methodology (supporting); Project administration (equal); Supervision (equal); Validation (supporting); Visualization (lead).

## REFERENCES

- <sup>1</sup>A. I. Selverston, “Invertebrate central pattern generator circuits,” *Phil. Trans. Roy. Soc. B: Biol. Sci.* **365**(1551), 2329–2345 (2010).
- <sup>2</sup>P. S. Katz, “Evolution of central pattern generators and rhythmic behaviours,” *Philos. Trans. R. Soc. London, Ser. B* **371**, 20150057 (2016).
- <sup>3</sup>A. Selverston, *Model Neural Networks and Behavior* (Springer Science & Business Media, 2013).
- <sup>4</sup>R. J. Calin-Jageman, M. J. Tunstall, B. D. Mensh, P. S. Katz, and W. N. Frost, “Parameter space analysis suggests multi-site plasticity contributes to motor pattern initiation in tritonia,” *J. Neurophysiol.* **98**, 2382–2398 (2007).
- <sup>5</sup>T. Bal, F. Nagy, and M. Moulins, “The pyloric central pattern generator in crustacea: A set of conditional neuronal oscillators,” *J. Comp. Physiol. A* **163**, 715–727 (1988).
- <sup>6</sup>E. Marder and R. L. Calabrese, “Principles of rhythmic motor pattern generation,” *Physiol. Rev.* **76**, 687–717 (1996).
- <sup>7</sup>R. Yuste, J. N. MacLean, J. Smith, and A. Lansner, “The cortex as a central pattern generator,” *Nat. Rev. Neurosci.* **6**, 477–483 (2005).
- <sup>8</sup>E. Marder and D. Bucher, “Central pattern generators and the control of rhythmic movements,” *Curr. Biol.* **11**, R986–R996 (2001).
- <sup>9</sup>P. A. Guertin, “Central pattern generator for locomotion: Anatomical, physiological, and pathophysiological considerations,” *Front. Neurol.* **3**, 183 (2013).

- <sup>10</sup>S. Grillner, Ö. Ekeberg, A. El Manira, A. Lansner, D. Parker, J. Tegner, and P. Wallen, "Intrinsic function of a neuronal network—a vertebrate central pattern generator," *Brain Res. Rev.* **26**, 184–197 (1998).
- <sup>11</sup>H. Nishimaru and N. Kudo, "Formation of the central pattern generator for locomotion in the rat and mouse," *Brain Res. Bull.* **53**, 661–669 (2000).
- <sup>12</sup>R. M. Harris-Warrick, "Neuromodulation and flexibility in central pattern generator networks," *Curr. Opin. Neurobiol.* **21**, 685–692 (2011).
- <sup>13</sup>J. Rubin and D. Terman, "Geometric analysis of population rhythms in synaptically coupled neuronal networks," *Neural Comput.* **12**, 597–645 (2000).
- <sup>14</sup>F. Skinner, L. Zhang, J. P. Velazquez, and P. Carlen, "Bursting in inhibitory interneuronal networks: A role for gap-junctional coupling," *J. Neurophysiol.* **81**, 1274–1283 (1999).
- <sup>15</sup>N. Kopell and B. Ermentrout, "Chemical and electrical synapses perform complementary roles in the synchronization of interneuronal networks," *Proc. Natl. Acad. Sci.* **101**, 15482–15487 (2004).
- <sup>16</sup>C. Canavier, D. Baxter, J. Clark, and J. Byrne, "Multiple modes of activity in a model neuron suggest a novel mechanism for the effects of neuromodulators," *J. Neurophysiol.* **72**, 872–882 (1994).
- <sup>17</sup>F. Skinner, N. Kopell, and E. Marder, "Mechanisms for oscillation and frequency control in networks of mutually inhibitory relaxation oscillators," *J. Comput. Neurosci.* **1**, 69–87 (1994).
- <sup>18</sup>A. A. Prinz, C. P. Billimoria, and E. Marder, "Alternative to hand-tuning conductance-based models: Construction and analysis of databases of model neurons," *J. Neurophysiol.* **90**(6), 3998–4015 (2003).
- <sup>19</sup>R. Dror, C. C. Canavier, R. J. Butera, J. W. Clark, and J. H. Byrne, "A mathematical criterion based on phase response curves for stability in a ring of coupled oscillators," *Biol. Cybern.* **80**, 11–23 (1999).
- <sup>20</sup>M. Madadi Asl, A. Valizadeh, and P. A. Tass, "Dendritic and axonal propagation delays may shape neuronal networks with plastic synapses," *Front. Physiol.* **9**, 1849 (2018).
- <sup>21</sup>H. Yu, K. Li, X. Guo, J. Wang, B. Deng, and C. Liu, "Firing rate oscillation and stochastic resonance in cortical networks with electrical–chemical synapses and time delay," *IEEE Trans. Fuzzy Syst.* **28**, 5–13 (2018).
- <sup>22</sup>Ö. Ekeberg, P. Wallén, A. Lansner, H. Tråvén, L. Brodin, and S. Grillner, "A computer based model for realistic simulations of neural networks: I. The single neuron and synaptic interaction," *Biol. Cybern.* **65**, 81–90 (1991).
- <sup>23</sup>H. Lim and Y. Choe, "Facilitating neural dynamics for delay compensation and prediction in evolutionary neural networks," in *Proceedings of the 8th Annual Conference on Genetic and Evolutionary Computation* (ACM, 2006), pp. 167–174.
- <sup>24</sup>H. Abarbanel, M. I. Rabinovich, A. Selverston, M. Bazhenov, R. Huerta, M. Sushchik, and L. Rubchinskii, "Synchronisation in neural networks," *Phys.-Usp.* **39**, 337 (1996).
- <sup>25</sup>H. Yu, X. Guo, J. Wang, K. Li, B. Deng, X. Wei, and C. Liu, "Multiple stochastic resonances and oscillation transitions in cortical networks with time delay," *IEEE Trans. Fuzzy Syst.* **28**, 39–46 (2018).
- <sup>26</sup>S. Li, G. Zhang, J. Wang, Y. Chen, and B. Deng, "Emergent central pattern generator behavior in chemical coupled two-compartment models with time delay," *Physica A* **491**, 177–187 (2018).
- <sup>27</sup>B. J. Norris, A. Wenning, T. M. Wright, and R. L. Calabrese, "Constancy and variability in the output of a central pattern generator," *J. Neurosci.* **31**, 4663–4674 (2011).
- <sup>28</sup>J. Santos and P. Fernández, "Evolution of synaptic delay based neural controllers for implementing central pattern generators in hexapod robotic structures," in *International Work-Conference on the Interplay Between Natural and Artificial Computation* (Springer, 2015), pp. 30–40.
- <sup>29</sup>C. Von Euler, "On the central pattern generator for the basic breathing rhythmicity," *J. Appl. Physiol.* **55**, 1647–1659 (1983).
- <sup>30</sup>T. G. Bautista, Q.-J. Sun, and P. M. Pilowsky, "The generation of pharyngeal phase of swallow and its coordination with breathing: Interaction between the swallow and respiratory central pattern generators," *Prog. Brain Res.* **212**, 253–275 (2014).
- <sup>31</sup>M. Dhamala, V. K. Jirsa, and M. Ding, "Enhancement of neural synchrony by time delay," *Phys. Rev. Lett.* **92**, 074104 (2004).
- <sup>32</sup>D. Maia, J. Kurths, and S. Yanchuk, "Stabilization of synchronous equilibria in regular dynamical networks with delayed coupling," *Nonlinear Dyn.* **111**, 7377–7390 (2023).
- <sup>33</sup>O. V. Popovych, S. Yanchuk, and P. A. Tass, "Delay-and coupling-induced firing patterns in oscillatory neural loops," *Phys. Rev. Lett.* **107**, 228102 (2011).
- <sup>34</sup>L. Kusch, M. Breyton, D. Depannemaecker, S. Petkoski, and V. K. Jirsa, "Synchronization in spiking neural networks with short and long connections and time delays," *Chaos* **35**, 013161 (2025).
- <sup>35</sup>J. Foss and J. Milton, "Multistability in recurrent neural loops arising from delay," *J. Neurophysiol.* **84**, 975–985 (2000).
- <sup>36</sup>Z. Song and J. Xu, "Multiple switching and bifurcations of in-phase and anti-phase periodic orbits to chaotic coexistence in a delayed half-center cpg oscillator," *Nonlinear Dyn.* **111**, 16569–16584 (2023).
- <sup>37</sup>J. Ma and J. Wu, "Multistability in spiking neuron models of delayed recurrent inhibitory loops," *Neural Comput.* **19**, 2124–2148 (2007).
- <sup>38</sup>Z. Song, J. Zhu, and J. Xu, "Gaits generation of quadruped locomotion for the CPG controller by the delay-coupled VDP oscillators," *Nonlinear Dyn.* **111**, 18461–18479 (2023).
- <sup>39</sup>C. P. Santos, N. Alves, and J. C. Moreno, "Biped locomotion control through a biomimetic CPG-based controller," *J. Intell. Rob. Syst.* **85**, 47–70 (2017).
- <sup>40</sup>P. Browne, E. Momoni, and F. Mahomed, "A generalized Fitzhugh–Nagumo equation," *Nonlinear Anal. Theory Methods Appl.* **68**, 1006–1015 (2008).
- <sup>41</sup>T. Carletti and H. Nakao, "Turing patterns in a network-reduced Fitzhugh–Nagumo model," *Phys. Rev. E* **101**, 022203 (2020).
- <sup>42</sup>I. T. Nkouna, Y. Xia, S. Yanchuk, R. Yamapi, and J. Kurths, "Generalized Fitzhugh–Nagumo model with tristable dynamics: Deterministic and stochastic bifurcations," *Chaos, Solitons Fractals* **175**, 114020 (2023).
- <sup>43</sup>J. Collens, K. Pusuluri, A. Kelley, D. Knapper, T. Xing, S. Basodi, D. Alacam, and A. Shilnikov, "Dynamics and bifurcations in multistable 3-cell neural networks," *Chaos* **30**, 072101 (2020).
- <sup>44</sup>J. Wojcik, R. Clewley, and A. Shilnikov, "Order parameter for bursting polyrhythms in multifunctional central pattern generators," *Phys. Rev. E* **83**, 056209 (2011).
- <sup>45</sup>J. E. Rubin and D. Terman, "Explicit maps to predict activation order in multiphase rhythms of a coupled cell network," *J. Math. Neurosci.* **2**, 4–28 (2012).
- <sup>46</sup>K. L. Briggman and W. Kristan, Jr., "Multifunctional pattern-generating circuits," *Annu. Rev. Neurosci.* **31**, 271–294 (2008).
- <sup>47</sup>J. T. Schwabedal, D. E. Knapper, and A. L. Shilnikov, "Qualitative and quantitative stability analysis of penta-rhythmic circuits," *Nonlinearity* **29**, 3647 (2016).
- <sup>48</sup>A. Shilnikov, R. Gordon, and I. Belykh, "Polyrhythmic synchronization in bursting networking motifs," *Chaos* **18**, 037120 (2008).
- <sup>49</sup>J. Wojcik, J. Schwabedal, R. Clewley, and A. L. Shilnikov, "Key bifurcations of bursting polyrhythms in 3-cell central pattern generators," *PLoS One* **9**, e92918 (2014).
- <sup>50</sup>M. L. Kolomiets and A. L. Shilnikov, "Poincaré return maps in neural dynamics: Three examples," in *Progress on Difference Equations and Discrete Dynamical Systems: 25th ICDEA, London, UK, 24–28 June 2019* (Springer, 2020), pp. 45–57.
- <sup>51</sup>V. Baruzzi, M. Lodi, M. Storace, and A. L. Shilnikov, "Generalized half-center oscillators with short-term synaptic plasticity," *Phys. Rev. E* **102**, 032406 (2020).
- <sup>52</sup>A. Kelley and A. Shilnikov, "2  $\theta$ -burster for rhythm-generating circuits," *Front. Appl. Math. Stat.* **6**, 588904 (2020).
- <sup>53</sup>R. Barrio, M. Rodriguez, S. Serrano, and A. Shilnikov, "Mechanism of quasi-periodic lag jitter in bursting rhythms by a neuronal network," *Europhys. Lett.* **112**, 38002 (2015).
- <sup>54</sup>J. Scully, J. Bourahmah, D. Bloom, and A. L. Shilnikov, "Pairing cellular and synaptic dynamics into building blocks of rhythmic neural circuits. A tutorial," *Front. Network Physiol.* **4**, 1397151 (2024).
- <sup>55</sup>L. Shilnikov, A. Shilnikov, D. Turaev, and L. Chua, *Methods of Qualitative Theory in Nonlinear Dynamics* (World Scientific, 2001), Vol. 5.
- <sup>56</sup>T. Brabec and F. Krausz, "Intense few-cycle laser fields: Frontiers of nonlinear optics," *Rev. Mod. Phys.* **72**, 545–591 (2000).
- <sup>57</sup>E. Goulielmakis, M. Schultze, M. Hofstetter, V. S. Yakovlev, J. Gagnon, M. Uiberacker, A. L. Aquila, E. Gullikson, D. T. Attwood, R. Kienberger *et al.*, "Single-cycle nonlinear optics," *Science* **320**, 1614–1617 (2008).
- <sup>58</sup>T. Kee, P. Sanda, N. Gupta, M. Stopfer, and M. Bazhenov, "Feed-forward versus feedback inhibition in a basic olfactory circuit," *PLoS Comput. Biol.* **11**, e1004531 (2015).

<sup>59</sup>A. T. Spröwitz, M. Ajallooeian, A. Tuleu, and A. J. Ijspeert, “Kinematic primitives for walking and trotting gaits of a quadruped robot with compliant legs,” *Front. Comput. Neurosci.* **8**, 27 (2014).

<sup>60</sup>M. Lodi, A. L. Shilnikov, and M. Storace, “Design principles for central pattern generators with preset rhythms,” *IEEE Trans. Neural Netw. Learn. Syst.* **31**, 3658–3669 (2019).

<sup>61</sup>P. Eckert, A. Spröwitz, H. Witte, and A. J. Ijspeert, “Comparing the effect of different spine and leg designs for a small bounding quadruped robot,” in *2015*

*IEEE International Conference on Robotics and Automation (ICRA)* (IEEE, 2015), pp. 3128–3133.

<sup>62</sup>K. Pusuluri, S. Basodi, and A. Shilnikov, “Computational exposition of multi-stable rhythms in 4-cell neural circuits,” *Commun. Nonlinear Sci. Numer. Simul.* **83**, 105139 (2020).

<sup>63</sup>J. Zang, S. Liu, P. Helson, and A. Kumar, “Structural constraints on the emergence of oscillations in multi-population neural networks,” *eLife* **12**, RP88777 (2024).